
Seeing the Wind: Visual Wind Speed Prediction with a Coupled Convolutional and Recurrent Neural Network

Jennifer L. Cardona

Department of Mechanical Engineering
Stanford University
Stanford, CA 94305
jcard27@stanford.edu

Michael F. Howland

Department of Mechanical Engineering
Stanford University
Stanford, CA 94305
mhowland@stanford.edu

John O. Dabiri

Department of Civil & Environmental Engineering
and Mechanical Engineering
Stanford University
Stanford, CA 94305
jodabiri@stanford.edu

Abstract

Wind energy resource quantification, air pollution monitoring, and weather forecasting all rely on rapid, accurate measurement of local wind conditions. Visual observations of the effects of wind—the swaying of trees and flapping of flags, for example—encode information regarding local wind conditions that can potentially be leveraged for visual anemometry that is inexpensive and ubiquitous. Here, we demonstrate a coupled convolutional neural network and recurrent neural network architecture that extracts the wind speed encoded in visually recorded flow-structure interactions of a flag in naturally occurring wind. Predictions for wind speeds ranging from 0.75-11 m/s showed agreement with measurements from a cup anemometer on site, with a root-mean-square error approaching the natural wind speed variability due to atmospheric turbulence. Generalizability of the network was demonstrated by successful prediction of wind speed based on recordings of other flags in the field and in a controlled in wind tunnel test. Furthermore, physics-based scaling of the flapping dynamics accurately predicts the dependence of the network performance on the video frame rate and duration.

1 Introduction

The ability to accurately measure wind speeds is important across several applications including locating optimal sites for wind turbines, estimating pollution dispersion, and storm tracking. Currently, taking these measurements requires placing a physical instrument at the exact location of interest, which can be cost prohibitive and in some cases unfeasible. Knowledge of the wind resource in cities is of particular interest as urbanization draws a larger portion of the world’s population to such areas, driving the need for more distributed energy generation closer to densely populated areas [16]. There is also burgeoning interest in the use of drones for delivery, which would greatly benefit from instantaneous knowledge of the local wind conditions to minimize energy consumption and ensure safety [24]. Here we demonstrate a technique that enables wind speed measurements to be made from a time series of images of flapping flags. This facilitates visual anemometry using pre-existing features in an environment, which would be non-intrusive and cost effective for wind mapping.

The flow-structure interaction between a flag and the wind encodes information about the wind speed. Neural networks can potentially be used to decode this information. Here, we leverage both physics and machine learning to predict wind speeds based on these interactions. The general approach to the current problem uses a convolutional neural network (CNN) as a feature extractor on each frame in a sequence, followed by a recurrent neural network (RNN) taking in the features extracted from the time series of frames. The input to our algorithm is a two-second video clip (a sequence of 30 images), and the output is a wind speed prediction in meters per second (m/s).

2 Related Work

There has long been interest in the use of neural networks in predicting future wind speeds based on historical measurements [19]. Much of the work in this area has been focused on wind forecasting (predicting future wind speeds) using time series of measurements from existing instrumentation or weather forecast data as inputs [3, 18, 4, 9, 2, 6]. Deep learning has recently been employed for meteorological precipitation nowcasting, where the authors used spatiotemporal radar echo data to make short-term rainfall intensity predictions using a convolutional LSTM [22]. The innovation proposed in this study is to use videos observing flow-structure interactions to make wind speed predictions without using any classical meteorological measurements as inputs. This enables wind speed prediction in a much broader range of physical environments, especially those where meteorological sensors would be expensive or impractical to install.

Recent work has shown success in classifying actions and motion in video clips using deep networks. While the current problem of predicting wind speeds using video clips has not been attempted, the present work draws inspiration from previous studies aimed at classifying videos. In the deep learning era, a number of approaches to video classification have arisen using deep networks. Three notable strategies that have taken hold include 3D convolutional networks over short clips [1, 15, 17, 25], two-stream networks aiming to extract context and motion information from separate streams [23], and the combination of 2D convolutional networks with subsequent recurrent layers to treat multiple video frames as a time series [8, 20]. Carreia *et al.* performed a comparison of these different approaches to video classification on currently available video datasets [5]. The present work will employ a strategy using a 2D CNN followed by long short-term memory (LSTM) layers. This approach leverages transfer learning on a CNN to extract features related to the instantaneous state of a flag, and an RNN to analyze the wind-induced flapping motion. Further discussion of this architecture choice can be found in Section 4.

3 Dataset

The main dataset used for training and validation consisted of videos taken at a field site in Lancaster, CA over the course of 20 days during August, 2018. Videos captured the motion of a standard checkerboard flag with an aspect ratio of 5:3 and size of 1.5 m \times 0.9 m mounted at 3 m height. Videos were recorded at 15 frames per second. The videos were subsequently separated into two-second clips (30 sequential frames), which were formatted as RGB images cropped to 224 \times 224 pixels. Thus, each sample used as a model input consists of a time series of images of total size 30 \times 224 \times 224 \times 3. True 1-minute average wind speed labels were provided by an anemometer on site at 10 m height. Each image sequence was matched to a wind speed label using the timestamp of the first image in the series. All 60,628 two-second clips in the original dataset were allocated for training and validation sets (75% and 25% respectively).

The measured 1-minute averaged wind speeds ranged from 0-15.5 m/s. Notably, the natural distribution of wind speeds was not uniform over the time-period of data collection, with many more samples in the middle speed ranges than at the tails. Since the desired output of the model was predictions over a broad range of wind speeds, the wind speeds were binned in 0.25 m/s increments, and for each bin, samples in excess of 225 for the training set and 90 for the validation set were not used in order to provide a more even distribution of wind speeds. The resulting splits contained 10,490 samples for the training set, and 4,091 samples for the validation set. The final distributions for the training and validation splits are provided in the Supplementary Materials document.

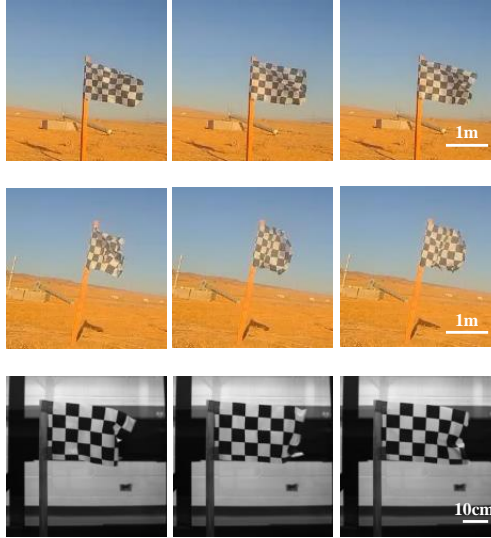


Figure 1: Example of sequential images of flag taken from a video clip (time sequence from left to right, with a timestep of $\frac{1}{15}$ s between each frame). Note that a full sample contains 30 frames, while only 3 are shown here for brevity. The three rows of frames refer to the (top) validation set, (center) adjacent flag test set, and (bottom) tunnel test set.

To assess the generalizability of the network, two test sets were collected containing videos of new flags in additional locations: a field test set (called the adjacent flag test set), and a wind tunnel test set (called the tunnel test set).

Adjacent Flag Test Set The adjacent flag test set comprised clips of a flag identical to the one used for training/validation. The test flag was located 3 m from the training/validation flag. Clips were taken at the same time as clips from the validation set to allow for direct comparison between validation results and test results on this new flag. Although the timestamps and wind speed labels are identical between the validation set and the adjacent flag test set, the precise wind conditions and corresponding flag motion differ between the two, as turbulence is chaotic and spatially heterogeneous.

Tunnel Test Set The tunnel test set consists of clips taken of a smaller checkered flag mounted in a wind tunnel. The tunnel flag had the same 5:3 aspect ratio as the other two flags discussed, but was size $0.37 \text{ m} \times 0.22 \text{ m}$. The wind tunnel was run at three speeds: $4.46 \pm 0.45 \text{ m/s}$, $5.64 \pm 0.45 \text{ m/s}$, $6.58 \pm 0.45 \text{ m/s}$. At each speed, 600 two-second clips were recorded at 15 frames per second, yielding 1,800 tunnel test samples. Although these videos were recorded on a monochrome camera, they were converted to 3-channel images by repeating the grayscale pixel values for each of the three channels for use in the model.

Example images from the validation set, adjacent flag test set, and tunnel test set are shown in Figure 1. The final dataset used in this work is available upon request.

4 Methods

4.1 Feature Extraction with ResNet-18

Before analyzing a video clip as a time series, each individual $224 \times 224 \times 3$ frame was fed through a 2D CNN to extract relevant features. The ResNet-18 architecture was chosen for the CNN because of its proven accuracy on previous tasks and relatively low computational cost [10]. Pre-trained weights for ResNet-18 were used in the current implementation to take advantage of transfer learning, available through the MathWorks Deep Learning Toolbox [14].

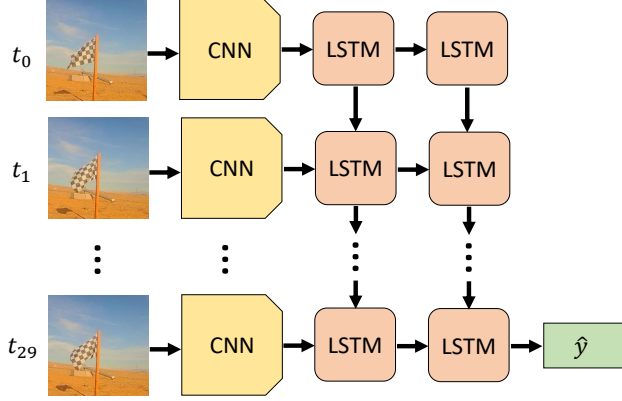


Figure 2: Schematic of the model architecture. The CNN is an ImageNet pre-trained ResNet-18 architecture [10]. The LSTM RNN is a many-to-one architecture with 2 layers each containing 1000 hidden units.

Since the purpose of the CNN here is feature extraction rather than image classification, the last two layers of the ResNet-18 (the fully connected layer and the softmax output layer) were removed so that the resulting output for each frame was a $7 \times 7 \times 512$ feature map. Since the activation function for the final layer was a rectified linear unit ($\text{ReLU}(x) = \max(0, x)$), many of the resulting features were zero. Therefore, to reduce memory constraints, the output features were fed through an additional maximum pooling layer with a filter size of 3 and a stride of 2. This acts to downsample the features and reduces the number of zeros in the dataset, reducing the feature map size to $3 \times 3 \times 512$ for each image, which was then flattened to $4,608 \times 1$. This resulted in a $4,608 \times 30$ output for each two-second (30 frame) clip to be used as an input for the recurrent network.

4.2 LSTM With and Without Mean Subtracted Inputs

Since flag flapping is inherently a temporal process, a RNN was selected in order to learn from these temporal features. The long short-term memory (LSTM) architecture was chosen due to its advantages in training over longer time series [12]. A generic LSTM cell is computed with the input, forget, output, and gate gates:

$$\begin{bmatrix} i \\ f \\ o \\ g \end{bmatrix} = \begin{bmatrix} \sigma \\ \sigma \\ \sigma \\ \tanh \end{bmatrix} W \begin{bmatrix} h_{t-1} \\ x_t \end{bmatrix}, \quad (1)$$

and the cell and hidden states are computed as Equations 2 and 3 respectively [12]:

$$c_t = f \odot c_{t-1} + i \odot g \quad (2)$$

$$h_t = o \odot \tanh(c_t). \quad (3)$$

The weight matrix W contains the learnable parameters. The sigmoid function, σ , is given by $\sigma(x) = e^x/(e^x + 1)$, and $\tanh(x) = (e^x - e^{-x})/(e^x + e^{-x})$. The LSTM is more easily trained on long sequences compared to standard RNNs because it is not susceptible to the problem of vanishing gradients, which arises due to successive multiplication by W during backpropagation through a standard RNN [11]. In a LSTM network, the cell state allows for uninterrupted gradient flow between memory cells during backpropagation, as it requires only multiplication by f rather than by W .

The ability to train on a relatively long time series is particularly important for our problem. As will be discussed further in the analysis of wind timescales in Section 5.1.1, the flapping of flags is inherently broadband, containing a broad range of spectral scales [26]. Typically, flags are located in the turbulent atmospheric boundary layer, where the length scales which govern the flow vary from

Table 1: Final hyperparameter choices for LSTM networks.

Hyperparameter	Chosen Value
# LSTM layers	2
# hidden units per LSTM layer	1000
learning rate	0.01

the order of kilometers to the order of micrometers. As a result, the associated time scales will range from very milliseconds to minutes. Therefore, the architecture chosen for this application should adapt to the variable spectral composition of the flow field, which is captured by the motion of the flapping flag. The LSTM network has the ability to learn a range of scales because of its inherent ability to use all points in a given time series.

As discussed in Section 4.1, the inputs to the LSTM network are obtained from the features extracted from the pre-trained ResNet-18 network. Since wind conditions are influenced by the diurnal cycle and other weather conditions [7], it is plausible that a model could use features present in the video clips other than the motion of the flag (e.g. the position of the sun, presence of clouds). To study and avoid such artifacts from overfitting to background conditions, two experiments were run using the same network architecture and hyperparameters, but trained using different inputs, referred to as LSTM-NM (short for no-mean) and LSTM-raw respectively.

LSTM-NM In this experiment, the temporal mean of each feature over the 30-frame clip was subtracted from the inputs to avoid fitting to background features. These mean-subtracted feature maps served as inputs for the LSTM network.

LSTM-raw Here, a second model was trained using the raw features extracted from the ResNet-18 model without mean subtraction. The main purpose of this experiment is to identify whether removing the temporal mean from a sequence is beneficial for model generalizability to new locations, and to confirm that it is in fact the flag motion that is used for predictions.

The LSTM architecture used here is many-to-one, since we have a series of 30 images being fed into the LSTM network with only one regression prediction being made. A schematic of the overall architecture is shown in Figure 2. Hyperparameters were chosen based on values used for other spatiotemporal tasks with a similar model architecture in the literature [27, 20, 8]. The final size of the LSTM network was chosen to be 2 layers with 1000 hidden units per layer. Two smaller models were also considered (1 layer with 10 hidden units, and 1 layer with 100 hidden units), but these models suffered from high bias, and were under-fitting the training set. A summary of the chosen hyperparameters is shown in Table 1.

4.3 Implementation Details

The mean-squared error was used as the loss function for this regression problem, defined as:

$$L = \frac{\sum_i^N (y_i - \hat{y}_i)^2}{N}, \quad (4)$$

where N is the number of training examples, y_i is the wind speed label, and \hat{y}_i is the predicted wind speed label for the given training example. Mean-squared error was chosen over mean absolute error to more heavily penalize outliers, which are particularly undesirable in applications related to wind energy due to the cubic dependence of wind power on wind speed.

Stochastic gradient descent with momentum was used for optimization, with a typical momentum parameter of 0.9 [21]. The algorithm was implemented using the MATLAB Deep Learning Toolbox [13]. The LSTM network was trained for 20 epochs using minibatches of 256 samples. This amount of training was sufficient to overfit to the training set within the limit of natural wind speed variability due to turbulence. Early stopping was employed for regularization. Computations were performed on a single CPU.

Table 2: Error metrics for validation and test cases. ‘Overall RMSE’ indicates the RMSE over all wind speeds, and ‘Measurable Range RMSE’ refers to the RMSE for wind speeds ranging from 0.75-11 m/s (described in Section 5.1.1).

Dataset	LSTM-raw RMSE (m/s)		LSTM-NM RMSE (m/s)	
	Overall	Measurable Range	Overall	Measurable Range
Validation Set	1.45	1.41	1.43	1.39
Adjacent Flag Test Set	2.68	3.03	2.95	1.81
Tunnel Test Set	N/A	6.54	N/A	1.35

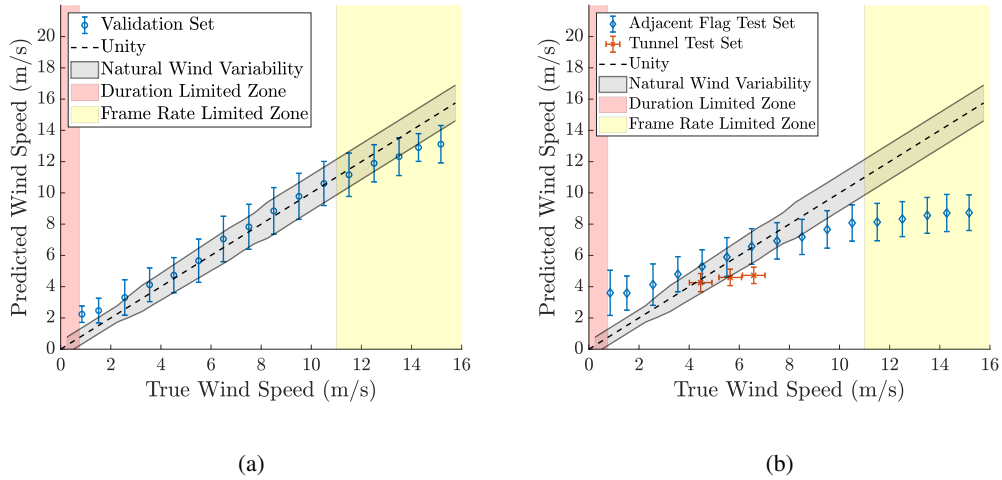


Figure 3: Mean LSTM-NM model predictions as a function of the true wind speed label for (a) the validation set and (b) the test sets. A perfect model would carry a one-to-one ratio, indicated by the ‘Unity’ line overlaid on the plot (dashed black line). Vertical error bars indicate one standard deviation. Horizontal error bars on the tunnel test set show the measurement uncertainty for the true wind speed labels. The wind speeds outside of the measurable range due to clip duration and frame rate are shown by the shaded red and yellow shaded regions respectively.

5 Results and Discussion

5.1 LSTM-NM Validation Results

Figure 3a shows the mean wind speed predictions for 1 m/s bins plotted against the true 1-minute average wind speed labels for the validation set. The error bars represent the standard deviation for each bin. The overall root-mean-squared error (RMSE) for the validation set was 1.43 m/s, which approaches the natural wind variability due to atmospheric turbulence as will be discussed in Section 5.1.2. The mean prediction for each bin shows good agreement with the true labels, but the model tends to under-predict for high wind speeds ($\bar{U} > 11$ m/s), and over-predict for low wind speeds ($\bar{U} < 2$ m/s). Although some of error at low wind speeds might be due to a lack of training examples in that range (see the training distribution in the Supplementary Materials document), as discussed in detail in the next section, we found that the reduced accuracy at the lowest and highest wind speeds could be predicted based on knowledge of the physics of the flow-structure interaction, as well as the video sample duration and temporal resolution.

5.1.1 Measurement Limitations at High and Low Wind Speeds

At the lowest and highest wind speeds tested, the increased prediction error can be explained by an inability of the current dataset to capture the relevant physics necessary to measure the wind speed. Specifically the pertinent physics are captured by a frequency scale of order f where,

$$f = U/L \quad (5)$$

is the frequency corresponding to a fluid element passing by the flag, L is the length of the flag, and U is the wind speed.

At high wind speeds the measurement capabilities are limited by the sampling rate, f_s . The Nyquist frequency, defined as $f_{Nyquist} = 0.5f_s$, is the highest frequency that a signal can have and still be observed without the effects of aliasing. Using the Nyquist frequency as an upper bound for the characteristic frequency, the corresponding critical velocity, $U_{c,high}$ can be calculated as:

$$U_{c,high} = Lf_{Nyquist} \quad (6)$$

In this case, $f_s = 15$ Hz, given by the frame rate, yields a Nyquist frequency of $f_{Nyquist} = 7.5$ Hz. The length of the flag is fixed at $L = 1.5$ m. Applying these values to Equation 6 gives $U_{c,high} = 11$ m/s. For wind speeds exceeding this value, the characteristic frequency would not be measurable without aliasing. This appears to manifest as an under-prediction at high wind speed values in Figure 3a.

At low wind speeds, the duration of clips, T , is the limiting factor. The lowest frequency that can be fully observed is $f = 1/T$. The critical velocity is then given by:

$$U_{c,low} = L/T \quad (7)$$

Given a clip length of 2 seconds, $U_{c,low} = 0.75$ m/s. Wind speeds lower than that would have fundamental frequencies that are too low to fully observe. Because of these known limitations for model performance at speeds under 0.75 m/s and above 11 m/s, the RMSE for range 0.75-11 m/s (hereafter referred to as the measurable wind speed range) has been reported in addition to the overall RMSE. For the validation set, the RMSE within this range was 1.39 m/s (results summarized in Table 2). The red and yellow shaded regions in Figure 3 indicate wind speeds outside of this measurable range due to duration and sampling rate respectively.

5.1.2 Comparison to Turbulent Fluctuations

In evaluating model performance, it is important to consider the natural variation in the wind speed due to turbulence. The minimum expected RMSE for model predictions is equal to the standard deviation of the turbulence fluctuations over a given averaging time (denoted σ_u). The fluctuating velocity, u' , and σ_u are given in Equations 8 and 9 respectively:

$$u' = u(t) - \bar{U} \quad (8)$$

$$\sigma_u = \sqrt{\bar{u'^2}} \quad (9)$$

where $u(t)$ is the instantaneous velocity, and \bar{U} is the time-averaged velocity. To calculate σ_u for our field site, 2-second average wind speed measurements were used to represent the instantaneous velocity, $u(t)$, and 1-minute average wind speed measurements were used for the mean velocity, \bar{U} . 2-second averages were used in order to match the duration of the video clips used as model inputs. 1-minute average wind speeds were binned in 0.5 m/s increments, and the mean natural variability due to turbulence (σ_u) was calculated for each bin, represented by the gray band in Figure 3a. Almost all of the mean predictions fall within this band, and the size of error bars representing the standard deviation in predictions is approaching the size of the band. This result indicates that the model performance approaches the best possible accuracy given natural wind variability.

5.2 LSTM-NM Test Results and Model Generalizability

Model predictions for both the adjacent flag test set and the tunnel test set are plotted against true labels in Figure 3b. As discussed in Section 3, the adjacent flag test set serves as a direct comparison to the validation set. Although the model still captures the increasing trend, the over-predictions at high wind speeds and under-predictions at low wind speeds are more pronounced than they were for the validation set, visible in the flatter shape of the curve shown in Figure 3b. The RMSE in the measureable range is 1.81 m/s (Table 2).

The tunnel test set results are shown by the orange marks in Figure 3b. Similarly to the adjacent flag test set, the predictions for the tunnel test set capture the correct qualitative increasing trend, although the highest wind speed case appears to be under-predicted. The RMSE for the tunnel test set in the measurable range was 1.35 m/s.

For both test sets, the RMSE in the measurable wind speed range was close to the validation set (Table 2). This indicates that the current model has potential to make predictions for flags other than the one it has been trained on, and flags that exist in new locations. This suggests the possibility for generalizability of this type of model in new settings, and its potential for broader use in mapping wind speeds.

5.3 LSTM-raw Results and Effect of Mean Subtraction

As discussed in Section 4.2, the LSTM-raw experiment used the same model architecture and hyperparameters as the LSTM-NM experiment, but used raw inputs rather than inputs with temporal mean-subtracted inputs. The LSTM-raw model performed very similarly to the LSTM-NM model on the validation set, with RMSE values of 1.41 m/s and 1.39 m/s respectively (Table 2). However, it did notably worse on both test sets. For the adjacent flag test set, the LSTM-raw model gave a RMSE of 3.03 m/s in the measureable range compared to 1.81 m/s for the LSTM-NM model. For the tunnel test set, the LSTM-raw model gave a RMSE of 6.54 m/s, compared to 1.35 m/s for LSTM-NM. The decrease in performance on the test sets for the LSTM-raw model indicates that without a temporal mean subtraction, this model was unable to make accurate predictions for a flag in a new location with a different background.

6 Conclusion and Future Work

Here, a coupled CNN and RNN using the ResNet-18 and LSTM architectures was trained to successfully predict wind speeds within a range from 0.75-11 m/s, with prediction errors approaching the minimum expected error due to turbulence fluctuations on the validation set. Model performance on test sets consisting of new flags in additional locations suggests that such a model may generalize, and could therefore prove useful in measuring wind speeds in new environments. Using this data-driven approach to visual anemometry could offer significant benefits in applications such as mapping complex wind fields in urban environments, as it could cut down on the time and cost required to measure wind speeds at several locations, which is currently done by installing an instrument at each point of interest.

Although this study focused specifically on video clips of checkered flags, this approach to wind speed measurement can potentially generalize to other types of objects, including other types of flags as well as natural vegetation such as trees that interact with the surrounding wind. In addition to training on a broader dataset including a variety of objects, confidence in the potential for model generalization can be further improved given a deeper understanding of which relevant physics the model is using for prediction. Here we showed how the measurement capabilities of a model were limited by the fundamental frequency of the flag. Future work will focus on understanding which physics of the fluid structure interactions are extracted by the model, and are necessary for accurate predictions.

References

- [1] Moez Baccouche, Franck Mamalet, Christian Wolf, Christophe Garcia, and Atilla Baskurt. Sequential Deep Learning for Human Action Recognition. In *International Workshop on Human Behavior Understanding*, 2011.

[2] Thanasis G Barbounis, John B Theοcharis, Minas C Alexiadis, and Petros S Dokopoulos. Long-Term Wind Speed and Power Forecasting Using Local Recurrent Neural Network Models. *IEEE Transactions on Energy Conversion*, 21(1):273, 2006.

[3] Kanna Bhaskar and S. N. Singh. AWNN-Assisted Wind Power Forecasting Using Feed-Forward Neural Network. *IEEE Transactions on Sustainable Energy*, 3(2):306–315, 4 2012.

[4] Erasmo Cadenas and Wilfrido Rivera. Wind speed forecasting in three different regions of Mexico, using a hybrid ARIMA–ANN model. *Renewable Energy*, 35(12):2732–2738, 12 2010.

[5] João Carreira and Andrew Zisserman. Quo Vadis, Action Recognition? A New Model and the Kinetics Dataset. In *IEEE Conference on Computer Vision and Pattern Recognition*, 2017.

[6] Francesco Castellani, Massimiliano Burlando, Samad Taghizadeh, Davide Astolfi, and Emanuele Piccioni. Wind energy forecast in complex sites with a hybrid neural network and CFD based method. *Energy Procedia*, 45:188–197, 2014.

[7] Aiguo Dai and Clara Deser. Diurnal and semidiurnal variations in global surface wind and divergence fields. *Journal Of Geophysical Research*, 104(D24):109–125, 1999.

[8] Jeff Donahue, Lisa Anne Hendricks, Sergio Guadarrama, Marcus Rohrbach, Subhashini Venugopalan, Kate Saenko, and Trevor Darrell. Long-term Recurrent Convolutional Networks for Visual Recognition and Description. In *IEEE Conference on Computer Vision and Pattern Recognition*, 2015.

[9] Zhenhai Guo, Weigang Zhao, Haiyan Lu, and Jianzhou Wang. Multi-step forecasting for wind speed using a modified EMD-based artificial neural network model. *Renewable Energy*, 37(1):241–249, 1 2012.

[10] Kaiming He, Xiangyu Zhang, Shaoqing Ren, and Jian Sun. Deep Residual Learning for Image Recognition. In *IEEE Conference on Computer Vision and Pattern Recognition*, 2016.

[11] Sepp Hochreiter. The Vanishing Gradient Problem During Learning Recurrent Neural Nets and Problem Solutions. *International Journal of Uncertainty, Fuzziness and Knowledge-Based Systems*, 6(2):107–116, 1998.

[12] Sepp Hochreiter and Jj Urgen Schmidhuber. Long Short-Term Memory. *Neural Computation*, 9(8):1735–1780, 1997.

[13] The MathWorks Inc. Deep learning toolbox. <https://www.mathworks.com/products/deep-learning.html>, 2019.

[14] The MathWorks Inc. resnet18. <https://www.mathworks.com/help/deeplearning/ref/resnet18.html>, 2019.

[15] Shuiwang Ji, Wei Xu, Ming Yang, and Kai Yu. 3D Convolutional Neural Networks for Human Action Recognition. *IEEE Transactions on Pattern Analysis and Machine Intelligence*, 35(1):221–231, 1 2013.

[16] Daniel M Kammen and Deborah A Sunter. City-integrated renewable energy for urban sustainability. *Science (New York, N.Y.)*, 352(6288):922–8, 5 2016.

[17] Andrej Karpathy, George Toderici, Sanketh Shetty, Thomas Leung, Rahul Sukthankar, and Li Fei-Fei. Large-scale Video Classification with Convolutional Neural Networks. In *In Proceedings of the IEEE conference on Computer Vision and Pattern Recognition*, 2014.

[18] Gong Li and Jing Shi. On comparing three artificial neural networks for wind speed forecasting. *Applied Energy*, 87(7):2313–2320, 7 2010.

[19] Mohamed A Mohandes, Shafiqur Rehman, and Talal O Halawan1. A Neural Networks Approach For Wind Speed Prediction. *Renewable Energy*, 13(3):345–354, 1998.

[20] Yue-Hei Joe Ng, Matthew Hausknecht, Sudheendra Vijayanarasimhan, Oriol Vinyals, Rajat Monga, and George Toderici. Beyond Short Snippets: Deep Networks for Video Classification. In *IEEE Conference on Computer Vision and Pattern Recognition*, 2015.

[21] David E Rumelhart, Geoffrey E Hinton, and Ronald J Williams. Learning Internal Representations By Error Propagation. *Parallel distributed processing*, 1:318–362, 1986.

[22] Xingjian Shi, Zhourong Chen, Hao Wang, Dit-Yan Yeung, Wai-Kin Wong, and Wang-Chun Woo. Convolutional LSTM Network: A Machine Learning Approach for Precipitation Nowcasting. In *Advances in neural information processing systems*, 2015.

- [23] Karen Simonyan and Andrew Zisserman. Two-Stream Convolutional Networks for Action Recognition in Videos. In *Advances in neural information processing systems*, 2014.
- [24] Joshuah K Stolaroff, Constantine Samaras, Emma R O'Neill, Alia Lubers, Alexandra S Mitchell, and Daniel Ceperley. Energy use and life cycle greenhouse gas emissions of drones for commercial package delivery. *Nature Communications*, 9(1):409, 12 2018.
- [25] Du Tran, Lubomir Bourdev, Rob Fergus, Lorenzo Torresani, and Manohar Paluri. Learning Spatiotemporal Features with 3D Convolutional Networks. In *IEEE Conference on Computer Vision and Pattern Recognition*, 2015.
- [26] XIA Yang and M F Howland. Implication of Taylor's hypothesis on measuring flow modulation. *Journal of Fluid Mechanics*, 836:222–237, 2018.
- [27] Haiyang Yu, Zhihai Wu, Shuqin Wang, Yunpeng Wang, and Xiaolei Ma. Spatiotemporal Recurrent Convolutional Networks for Traffic Prediction in Transportation Networks. *Sensors*, 17, 2017.

Supplementary Materials

Jennifer L. Cardona
 Department of Mechanical Engineering
 Stanford University
 Stanford, CA 94305
 jcard27@stanford.edu

Michael F. Howland
 Department of Mechanical Engineering
 Stanford University
 Stanford, CA 94305
 mhowland@stanford.edu

John O. Dabiri
 Department of Civil & Environmental Engineering
 and Mechanical Engineering
 Stanford University
 Stanford, CA 94305
 jodabiri@stanford.edu

1 Wind Speed Distributions

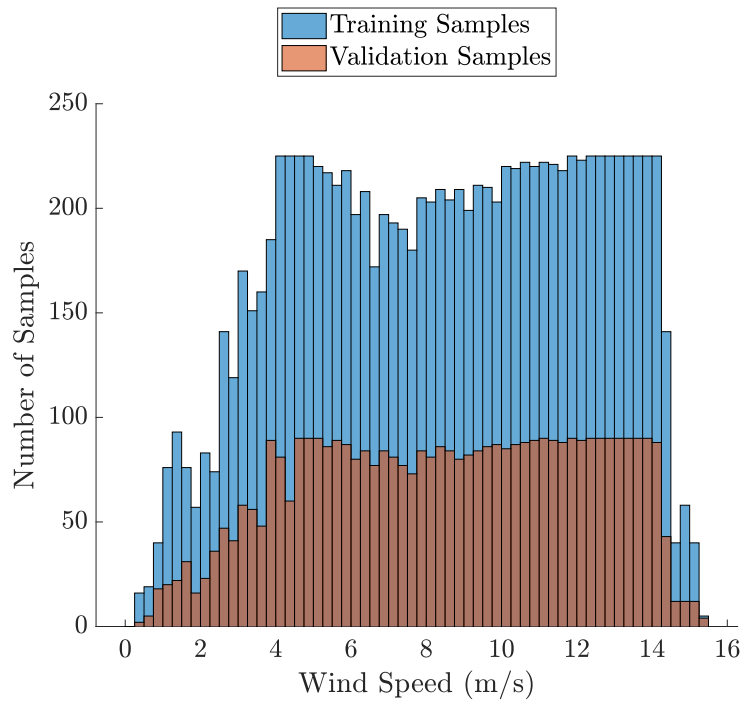


Figure 1: Final wind speed distributions used for the training and validation splits.